Design of a Microfluidics Device for Facile Processing of Encapsulated Stem Cells

Authors:

Timothy Boyer, Undergraduate Department of Biomedical Engineering
Melody Chiang, Undergraduate Department of Biomedical Engineering
Cole Latvis, Undergraduate Department of Biomedical Engineering

Word Count: 3745
Number of Figures: 7
Number of Tables: 1
Number of Equations: 1
Number of Supplements: 3
Number of References: 21

Approved: _____ Date: May 7, 2021

Christopher Highley, PhD, Department of Biomedical Engineering

Design of a Microfluidics Device for Facile Processing of Encapsulated Stem Cells

Timothy Boyer[a], Melody Chiang[a], Cole Latvis[a,1]

[a] Biomedical Engineering Undergraduate at the University of Virginia
[1] crl3ar@virginia.edu

Abstract

Age-related degenerative conditions, such as stroke and heart disease, have become the defining clinical challenges of our time. These conditions are associated with debilitating loss of tissue function and declines in quality of life. As the population ages, the impact of these conditions will continue to rise, necessitating the development of biomedical solutions like stem cell therapies. Stem cell therapies have the potential to restore tissue function lost from degenerative conditions, especially when cells can be efficiently sourced through allogeneic means. However, allogeneic cells commonly succumb to host immune responses before therapeutic benefit can be achieved. This report proposes a microfluidic design that may be used to encapsulate stem cells in biocompatible polymer layers. Drawing on previous research on inertial focusing, our device uses chambers of expanded width to generate vortices, which selectively trap large particles while allowing small particles to pass. This allows cells to be stably trapped without clogging, while sequential reagents are applied to encapsulate cells in a layer-by-layer manner. This process can be automated for high-throughput processing. To evaluate feasibility, computational fluid dynamics were applied to determine theoretical fluid parameters needed to generate specific flow characteristics. We found that models could be scaled to larger geometries using the channel Reynolds number while preserving relevant flow characteristics, which justified the use of scaled-up models as a platform for rapid prototyping. These 3D-printed prototypes quantitatively and qualitatively recapitulated the flow suggested by simulations, including flow rates and flow line curvature, but were not able to withstand high pressures necessary for vortex formation due to leaking of the device. As a result, these devices only represent a proof-of-concept for scaled-up 3D-printed devices. Lastly, we have designed a microfluidic device, based on these concepts, to be made out of PDMS using soft-lithography, a more robust fabrication material and method.

Keywords: microfluidics, layer-by-layer cell encapsulation, inertial focusing, 3D-printing, computational fluid dynamics modeling

Introduction

Each year, nearly 800,000 people experience a new or recurrent stroke, and 87% of all strokes are ischemic.[1] Ischemic stroke is a leading cause of death worldwide, with rates of morbidity only eclipsed by ischemic heart disease.[2] Of those who survive the initial episode, 40% become disabled and physiotherapy only offers modest recovery of lost motor functions.[2,3]

Stem cells, immature cells with the capacity for self-renewal and differentiation, are promising candidates for therapies to treat degenerative diseases like stroke.[4,5] Stem cell therapy, in particular, is well suited for stroke treatment due to its potential for replacing damaged cells in the brain and providing beneficial paracrine effects.[6] Various cell types, including rodent bone marrow mesenchymal cells and immortalized mouse neural precursor cells, have been transplanted into the brain in animal models of stroke and have been found to reduce neurological deficits following brain ischemia.[5,7] Transplanted stem cells can also secrete trophic factors like vascular endothelial growth factor, glial cell-derived neurotrophic factor, and fibroblast growth factor, that confer neuroprotective functions and promote enhanced recovery after stroke.[8]

The long time frame needed to produce sufficient numbers of autologous stem cells makes the transplantation of allogeneic stem cells an attractive alternative for the development of stem cell therapies. The main barriers to widespread clinical implementation of allogeneic cells, however, include appropriate delivery methods and immunogenicity. A proposed method for overcoming these obstacles is cell encapsulation, where cells are enclosed in a biocompatible matrix that can serve as a barrier to immune response or cytotoxic molecules.[9] Cell encapsulation reduces the likelihood for rejection while facilitating the diffusion of hormones, oxygen, and nutrients.[9] Several proof-of-concept studies in animal models have had initial success in using encapsulated stem cells in applications like glycemic correction in diabetes and therapy after myocardial infarction.[10,11]

Historically, bulk encapsulation using polymers like agarose, alginate, and hyaluronic acid (HA) is standard for cell encapsulation.[12] However, limitations of this method include short sustenance period, low permeability, and limited stability, highlighting a need for new encapsulation methods.[13] Bulk encapsulation limits the therapeutic benefit of the cells by preventing the diffusion of growth factors and other paracrine molecules. Furthermore, the bulky geometry complicates therapies that rely on intravenous injection and prevents precise placement of cells for therapies. To avoid these problems, layer-by-layer (LbL) single cell encapsulation, a method that facilitates multilamellar encapsulation through intermolecular interactions such as covalent bonding, hydrogen bonding and hydrophobic interactions, can be used.[13] This method allows for precise control over the thickness and biochemical properties of the polymer layers surrounding the cells, and thus diffusion rates to and from the cell.[9,13] LbL encapsulation can create

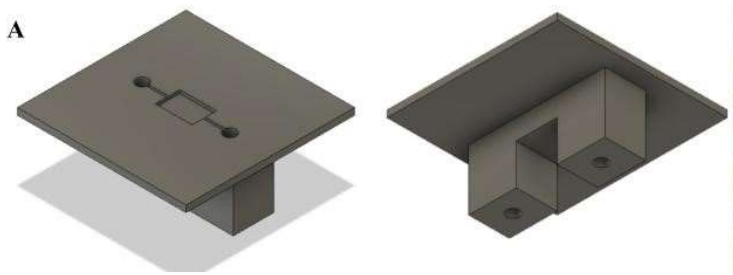

Fig. 1. Design of 3D-printed prototype. (A) Representative design created in AutoCAD with views from the top and bottom of the device. The inlet and outlet are visible on the bottom view. (B) Example of 3D-printed device with tubing connected to the inlet and outlet.

therapeutic materials with higher cell density due to the lack of excess material and are appropriate for intravenous-injection since the cells are not interconnected. However, LbL encapsulation can be improved upon as the process for encapsulating the cells is tedious and would be difficult to scale-up for larger manufacturing. To scale up production of encapsulated cells, a more efficient and high-throughput fabrication method is needed.

To address this problem, we aimed to design and develop a microfluidic device for the creation and purification of multilamellar HA-encapsulated stem cells. Microfluidic platforms, in particular, allow for precise control over particle size and monodispersity, making them desirable for microencapsulation.[14] Developing a procedure to encapsulate stem cells more efficiently will accelerate and increase the feasibility of the clinical implementation of stem cell therapies to treat stroke patients. Additionally, the procedure developed through this project is not limited to the encapsulation of stem cells solely for use in treating neurological disorders; treatments for a wide variety of other pathologies, including myocardial infarctions, diabetes, and liver disease, may also be accelerated by the development of our device. The potential uses of stem cell encapsulation technologies is not limited to stem cell therapy either, as applications include tissue engineering, drug delivery, and manipulation of cellular microenvironments. Therefore, this project will have far-reaching implications for treatment of degenerative diseases by offering insight into how cell encapsulation procedures can be improved.

The following aims guided the development of our device. Aim 1 involved determining the specifications of a microfluidic device that would best provide an effective and less-labor intensive cell encapsulation and separation process via literature review. Aim 2 involved the design and fabrication of the microfluidic device, and Aim 3 involved evaluating the efficacy of the fabricated device. Aims 2 and 3 specifically pertained to a scaled-up 3D printed version of our design. Overall, this project represents a first step proof-of-concept of a microfluidic device capable of cell encapsulation.

Results

Device Design

Past microfluidic devices have utilized a variety of techniques for particle separation including filtration, deterministic lateral displacement (DLD), hydrodynamic forces, and inertial focusing.[14,15] Filtration techniques incorporate geometries like pores, weirs, pillars, and crossflows, and take advantage of differences in cell size or deformation to achieve separation.[14] DLD is an application of filtration techniques and involves a large array of pillar structures that can separate particles over a wide range of sizes.[16] However, these techniques have a large number of physical structures that can lead to clogging issues.

Hydrodynamic forces involve a straight main channel with several side channels through which fluid is drained, and the positioning of differently-sized particles in different streamlines facilitates separation.[14] Hydrodynamic techniques allow for the use of wider channels, which minimize clogging and increase throughput.[16] Inertial focusing is a technique that takes advantage of competing inertial lift forces acting on particles in a microchamber to direct particle movement and form microscale vortices in which particles can be trapped.[17] Advantages of this technique include high-throughput, simple channel geometries, low cost, reduced clogging, and precise manipulation.[15] Each of these passive microfluidic techniques have not only been used individually, but also in combination. For example, a two-stage device that coupled inertial focusing with DLD was used to separate blood cells from tumor cells with a separation efficiency of over 99.9%.[18] Individual or a combination of microfluidic techniques were considered for the device design.

Ultimately, we decided the most important factors for our design were reduced clogging, continual flow encapsulation, and mass separation, making inertial focusing a desirable technique for our device design. Other benefits of inertial focusing include the ability to separate particles by size or density, concentrate samples, and facilitate solution exchange.[19] Mach et al. employed inertial focusing to separate and concentrate cancer cells from blood and found that vortex-trapped cells could be "washed" without disruption of the vortices.[19] This property of microvortices is especially useful for our desired application, where cells can be encapsulated with multiple layers of polymers. If vortex-trapped cells can be stably trapped, then multiple different polymers can be injected into the device sequentially with wash steps in between for layering. Additionally, Mach et al. was able to use inertial focusing to fluorescently label vortex-trapped cells via multiple solution exchanges with labeling agents and wash solutions, further suggesting that encapsulation of multiple layers of polymers is feasible.[19]

The basic unit in our design is a single inertial microfluidic chamber (Figure 1A), which is a region of expanded width meant to facilitate the formation of microvortices. Previous studies suggest workable dimensions feature 900x600x70 μm chambers and 50x70 μm channels. From this starting point, simple variants of the single chamber device were drafted, along with more complex designs. Our project mainly addresses whether particles can form vortices within a single chamber, using computational modeling and assessing fluid flow with a physical device. Informed by these tests, photomasks for soft-lithography were constructed with more complex features as described in the Microfluidics Designs for Soft-Lithography section.

Computational Fluid Dynamics Simulations

Simple models of the inertial microfluidic entrapment chambers were created in Autodesk Fusion 360 and analyzed in Autodesk CFD. Figure 2 shows the vector field for a simple single chamber model with inlet channel width of 50 μm and chamber size of 600x900x70 μm at a Reynolds number (Re_c) of 14, 80, and 166. It can be seen qualitatively that at low Re_c flow lines are bent, but there is no formation of vortices within the entrapment chamber. However, at a Re_c of 80 and 166 the phenomenon is seen, with larger and more defined vortices forming at

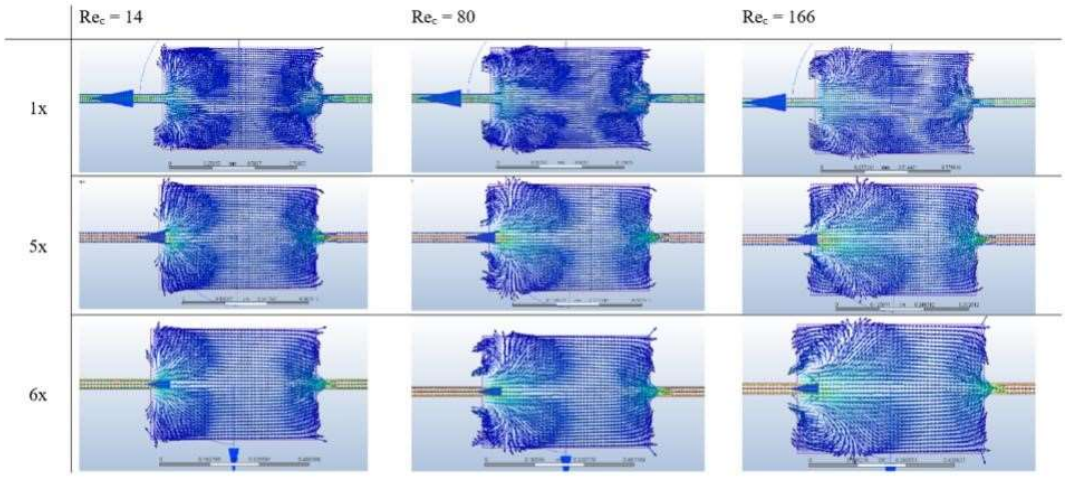

Fig. 2. Velocity vector fields computed for the basic inertial chamber geometry at different size scaling and Re_c. The columns represent Re_c values of 14, 80, and 166, and the rows represent different linear scaling (1x, 5x, and 6x) of the basic inertial chamber geometries fabricated and tested.

larger Re_c. It was further observed that vortex size correlates with the Re_c, as suggested by literature.[20] Further analysis confirmed the flow characteristics are consistent across chambers in series (Supplemental Figure S1), as expected by conservation of mass, suggesting that our basic design can be modified to include more complex structures and greater numbers of inertial chambers.

Along with the standard-sized model of the basic unit of the device, 5 and 6 times larger variants, as well as a 5 times scaled model with 10x deeper channels, were analyzed computationally (Figure 2). Although flow rates necessary for vortex formation differed, it was found that similar flow characteristics develop at the same Re_c values for linearly scaled models. However, for models with independently expanded depth, formation of vortices occurred at lower Re_c. This conservation of general flow characteristics with Re_c for the linearly scaled devices suggests that functional scaled-up models of the microfluidic designs can be created. This validated the use of 3D-printed scaled-up models as rapid prototypes.

Device Flow Experiments

To verify the predictive power of the CFD simulated flow, several 5 and 6 times scaled resin 3D-printed microfluidic devices were fabricated (Figure 1B) and the experimentally derived flow characteristics through these devices was compared against those of the simulation. To visualize and quantify the flow of particles through the printed systems, liquid mixtures containing hydrogel microbeads were perfused through the entrapment chambers under light microscopy. While identifying vortex formation would be ideal, increasing the volumetric flow rate to the necessary level, of around 135-215 cm^3/hr, according to the simulations, led to severe leaking of the 3D printed constructs. Both vacuum grease and silicone sealant were used to mount the 3D-printed device onto a glass slide, but neither could withstand the increased pressure associated with high fluid velocities without the seal rupturing and the device failing.

However, at lower flow rates, such as 34 cm^3/hr, individual representative particle tracking was performed using microscopy images. Then, these distances were compared to the computationally predicted particle flow rates at those areas (Table 1). Heat maps of absolute velocity within the chambers provided a quantitative characterization of the simulated flow and were used to determine the computationally predicted particle flow rates (Supplemental Figure S2; Table 1). For Particle Position 2, it was found that the computationally-derived speed lay within the 95% confidence interval established by experimental measurements, but for Particle Position 1, the computationally-derived speed exceeded the upper bound of the confidence interval. This may have been due to partial channel blockage by loose resin, causing some abnormal flow patterns during the experiment. Leakage of the device may have also reduced observed flow speeds.

Qualitative Assessment of Particle Flow Distribution

While it was not feasible to increase flow rates to those needed for vortex formation in the scaled-up models, representative images at a lower flow rate, 34 cm^3/hr, and low Re_c demonstrate similar flow profiles to computational models. Hydrogel particles demonstrate curved flow profiles immediately out of the inlet due to a dramatic increase in channel width (Figure 3A). While channel blockage from suspected loose resin shavings shifted the effective particle entrance to the left in Figure 3B (red arrow), a distinct flow bifurcation can be visualized (blue arrows), which is reminiscent of the flow pattern present in the computational simulations at low Re_c.

Although expected vortex formation could not be achieved, evidence of this phenomena was still observed in some cases. As seen at the top of Figure 4, unclearable air bubbles blocked the chamber and disrupted flow out of the inlet situated at the bottom right of each image. However, this inadvertent issue led to a decreased chamber size and increased pressure, which led to the visualization of suspected vortex formation based on the presence of backwards moving particles (Figure 4, blue arrows). Although this result should be taken lightly and may not be reproducible,

	Average Coordinates		Image-Derived Speed	95% CI for Image-Derived	Computationally-Derived Speed
	X	Y	cm/sec	cm/sec	cm/sec
Particle Position 1	-954.1667	1555.0000	0.3158 ± 0.0654	[0.1850 , 0.4466]	0.4925
Particle Position 2	752.5000	976.6667	0.3807 ± 0.0793	[0.2221 , 0.5393]	0.4425

Table 1. Comparison between image-derived (experimental) and computationally-derived (theoretical) flow rates for particles within the inertial chambers with 95% confidence intervals. Coordinates are defined in μm relative to the center of the inlet. Image-derived speed is reported with +/- 1 standard deviation.

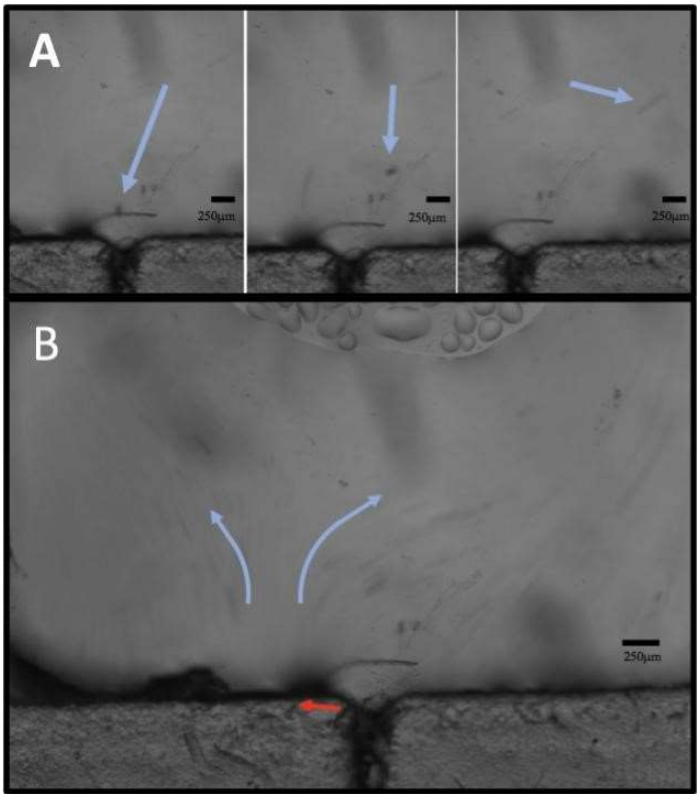

Fig. 3. Visualization of flows within the 3D-printed prototype. (A) Representative curved particle flowing out of the device inlet. (B) The flow profile out of the inlet demonstrates streamline bifurcation (blue arrows). Some particles out of inlet were displaced to the left due to inlet clogging (red arrow).

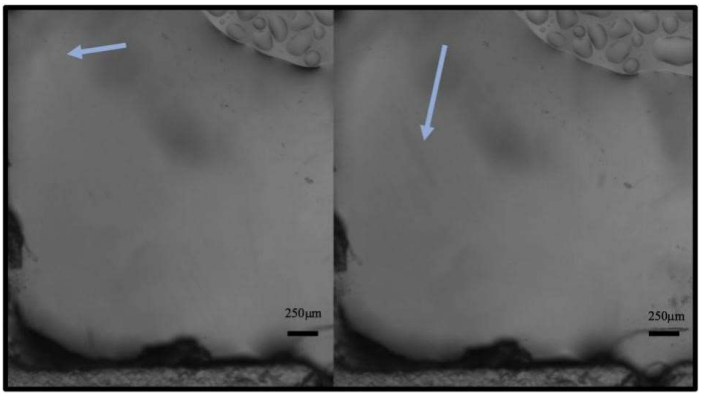

Fig. 4. Representative backward-moving particle, indicating potential vortex formation.

it does suggest that fluid flow under high pressure situations can lead to vortex formation in 3D printed devices. Moreover, it demonstrates that hydrogel microbeads may be used to visualize their formation. As a whole, the unreliability of these flow experiments with 3D-printed devices underscores the need for more durable, compact, and higher-resolution fabrication methods and materials for our microfluidic devices. Soft-lithography is a common method for printing micrometer-sized microfluidic devices. This technique can be used to create microfluidic devices using photosensitive materials to make a mold for the creation of microscale channels and chambers out of

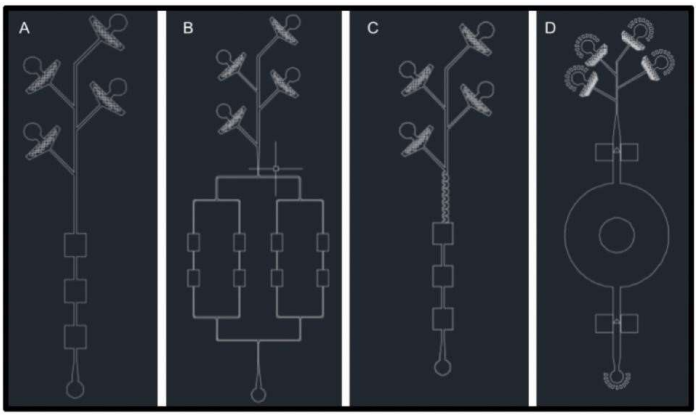

Fig. 5. Microfluidic device designs.

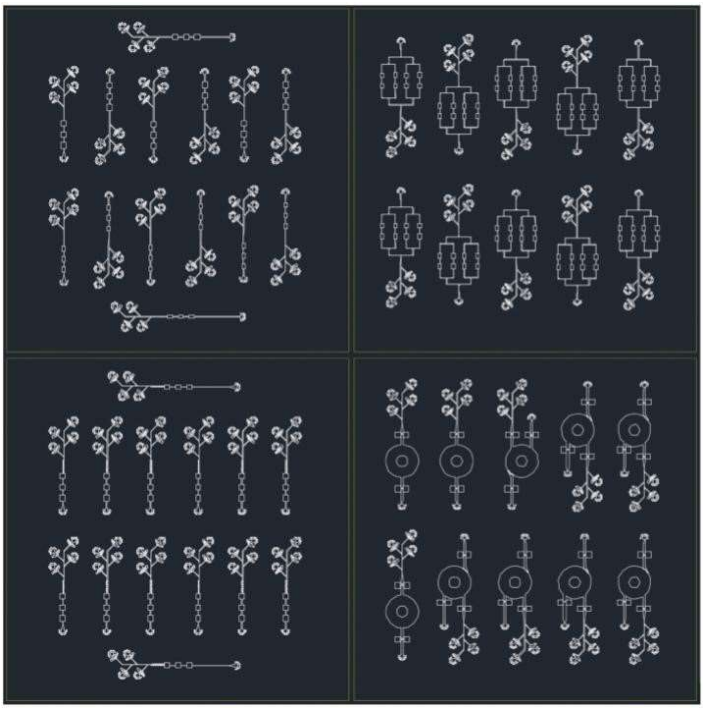

Fig. 6. Arranged microfluidic devices for soft-lithography fabrication.

polydimethylsiloxane (PDMS) plastic. PDMS devices allow for smaller detail, result in less leaking, and are more suitable for microflows.

Microfluidic Designs for Soft-Lithography

While restrictions with laboratory access during the pandemic prevented us from being trained to fabricate devices with soft-lithography, we used AutoCAD to make designs for a photomask that was constructed for eventual soft-lithography fabrication. In each device, the four inputs have a filter to capture fragments of PDMS that may dislodge during fabrication to prevent clogging of PDMS into the device. The first device consists of three 900x1000 μm inertial chambers arranged in series with 100 μm width channels (Figure 5A). The second device (not pictured) is identical to that in A but has 600x900 μm chambers and 50 μm width channels. Our third design combines 600x900 μm inertial chambers in series and in parallel (Figure 5B). Our fourth design is similar to that in Figure 6A, except it includes snake-like channels, a design proposed by Di Carlo et al.[20] (Figure 5C). The purpose of these snake-like channels is to focus particles in a linear arrangement. These channels are intended to

position particles in the center of the channel before entering the inertial chamber to promote more consistency when forming vortices. The fifth design uses an alternate method, where instead of trapping cells in vortices, semi-always-closed valves are used to trap cells in a reaction chamber while fluid flows past (Figure 5D). This concept is adapted from a previous microfluidic device created as a biosensor for heavy metal ions.[21] The devices were arranged on a 12.6 cm^2 slide (Figure 6) for future fabrication using soft-lithography.

Discussion

The development of a device for the facile processing of encapsulated cells has the potential to accelerate the translation and availability of stem cell based therapies by increasing the applicability of non-autologous stem cells. While standard methods of cell encapsulation are laborious and potentially damaging to the cell, the technology outlined in this work represents the first step towards a fully automated and high throughput apparatus for applying polymer coats. Although a fully functioning device was not created during this project, proof-of-concept was established computationally and with scaled-up models.

Stereolithography 3D-printing is an attractive manufacturing and prototyping method in the realm of microfluidic devices. The method creates non-porous structures with resolution in the tens to hundreds of microns in an automated and rapid manner. However, this method of construction can be less precise than soft lithography and, for some applications, the resolution is not small enough to adequately create fine structures. The latter concern prevented the printing of to-scale models of the device proposed in this work. Due to this, the use of stereolithography was not initially considered for this project. However, delays in training in soft-lithography led to a reconsideration. To use 3D-printing, the designs would need to be scaled up significantly, which had the potential to alter the flow characteristics through the systems.

Mach et al. demonstrated that vortex size in entrapment chambers had a positive correlation with the Re_c, however, the dependency on this parameter across size scales was not explored.[19] To determine a relationship between the Rec and vortex formation, velocity vector fields were generated for qualitative comparisons of flow characteristics of models of varying size but constant Re_c (Figure 2). It was found that linearly scaled geometries indeed conserve flow patterns across size scales. This justified the use of the scaled-up designs for prototyping as the devices would be expected to remain capable of vortex formation and particle entrapment, though with far larger volumes of fluid, less densely packed cells, and high fluid velocities. Interestingly, however, altering the depth of the device independently changes the relationship, where deeper channels produce vortices more readily at lower Re_c. This finding can be used to inform the relative depth and width that should be incorporated in the full-scale soft-lithography model.

We printed 5x and 6x scaled models of the inertial chambers. Although it was possible to connect these devices to a syringe pump and perfuse them with liquid, they would have required relatively high input flow speeds to form vortices according to the vector fields generated by AutoDesk CFD. The glass slide that sealed the functional component was held in place by only vacuum grease and mechanical clamping, and we observed that the device leaked at flow speeds well below the speeds necessary for vortex formation. The device would likely completely fail at desired flow rates. For later experiments silicone sealant was used, but this only brought marginal improvements in maximum tolerable flow rates, from 250 to 557 µL/min. In addition to leaking, clogging from vacuum grease or loose resin disrupted flow results as well. However, when flow could be properly established, the printed models recapitulated both qualitative and quantitative simulation flow characteristics as visualized by hydrogel beads (Figures 3 and 4). This provides a preliminary validation of the simulations and suggests the potential for 3D printed devices for inertial trapping applications is feasible given stronger and more consistent sealing procedures. Larger 3D-printed devices may be explored further in future work, but would require larger quantities of reagents due to more diffuse cell entrapment. However, for now, these limitations underscore the need for smaller scale devices that require lower forces to function. Overall, the results for the 3D-printed prototypes provide valuable insights for design of smaller full-scale devices.

A full-scale microfluidic device would not only require less expensive regents due its small size, it would also be fully sealed and require far lower forces to achieve vortex formation. For these reasons a microfluidic device created through soft-lithography was pursued. Although the proposed PDMS devices were not fully completed for this project, future Capstone students can use the photomask chip produced for this project as a starting point in continuing the development of a microfluidic device for cell encapsulation.

The next step for this project is to fabricate the set of microfluidic devices that are being created using soft-lithography. After fabrication and setup of the input and output flows, the first step would be to optimize the flow rates for these devices through both CFD simulations and experimentation. Experiments with fluorescent microbeads can be conducted to confirm the proper formation of vortices within the device. Afterwards, experiments with cells can be conducted as well, and another parameter that would need to be determined is the optimal concentration of cells to be flowed through the device. Once all those steps have been completed, cell encapsulation studies can be initiated.

Ultimately, if successful, this project will have resulted in the design and fabrication of a microfluidic device capable of high-throughput and automated cell encapsulation. This device will streamline the production of encapsulated stem cells and accelerate the development of stem cell therapies or any other applications where cell encapsulation is desired.

Materials and Methods

Device Design

The aim to create a microfluidic device imposed a number of inherent design constraints. The major technical constraint was resolution of the fabrication method. While the proposed microfluidic fabrication technique, soft-lithography, offers great precision, it is still limited to an approximately 10 µm resolution. Additionally, channel widths should not exceed the diameter of a neural stem cell, ~12 µm. As a second constraint, only passive microfluidic techniques that do not rely on extrinsic forces were considered. This choice both limited the complexity of the design process and enabled the simple application of flow simulation software.

In addition to these constraints, multiple design criteria are desirable in a microfluidic device design. These include simplicity, ease of use, minimal clogging, and potential for automation. More specific to microencapsulation, the device must be capable of both incubation with reagents and separation of encapsulated cells from monomer solutions. With these constraints and criteria as a guide, a literature review was undertaken to identify the type of microfluidic device that would be best suited for cell encapsulation. Once the general concept was determined, various potential device variants were modeled in computer-aided design

software, Autodesk AutoCAD and Autodesk Fusion 360, before a final general outline was established.

Computational Fluid Dynamics Simulations

To evaluate the flow characteristics through device designs, the Autodesk Fusion 360 models were uploaded to a computational fluid dynamics (CFD) software, Autodesk CFD. For each design, vector fields representing the fluid velocity projection onto the plane in the center of the inertial chambers were visualized. In addition, heat maps of absolute velocity within this plane were constructed. Representative images from each trial were captured for qualitative comparisons. Each device variant was evaluated at three channel Reynold's numbers (Re_c): 14, 80, and 166. Since the channels used were rectangular, Equation 1 was derived to calculate the Rec, where Q is the volumetric flow rate in cm^3/s, and A and B are the dimensions of the channel in cm (see Supplemental Figure S3 for full derivation).

$$Re_c = \frac{200Q}{A+B} \quad [1]$$

3D-Printed Prototypes

Prototype devices were 3D-printed in standard photopolymer resin using a Form Labs Form 2 stereolithography 3D-printer. Since standard sized models of the proposed device contain channels below the resolution of this printer, which is on the order of hundreds of microns, models scaled up linearly by 5 and 6 times were fabricated instead. Additionally, a 5 times scaled model was constructed with 10 times deeper channels than the original to prevent clogging from loose sealant. The design and setup of each 3D-printed device is seen in Figure 1. A 25x25x1 mm face plate acts as a platform for the embedding of channels, and is sealed against a 25x25 mm glass coverslip with vacuum grease or silicone sealant. Either end of the channels is connected to perpendicular 1.80 mm diameter cylindrical inlets and outlets that extend 9 mm below the faceplate. Here, threaded couplings connect the 3D-printed devices to tubing, which are connected to a syringe pump at the inlet, or a collection flask at the outlet. This connected system was placed onto a bright field microscope for analysis (Figure 7).

Each prototype was first perfused with tap water to establish flow through the channels and to expel air bubbles, before a solution containing hydrogel beads 5-20 μm in diameter was added, which allowed for visualization and quantification of flow characteristics. Volumetric flow rates of 15 and 34 cm^3/hr were applied to the device variants. The bright field microscope captured images at 4 frames per second, which were converted to 25 frames per second videos. At specific locations within the inertial chamber, particle speed was quantified using ImageJ to determine the distance a particle travelled from one frame to the next (a period of 0.25 seconds).

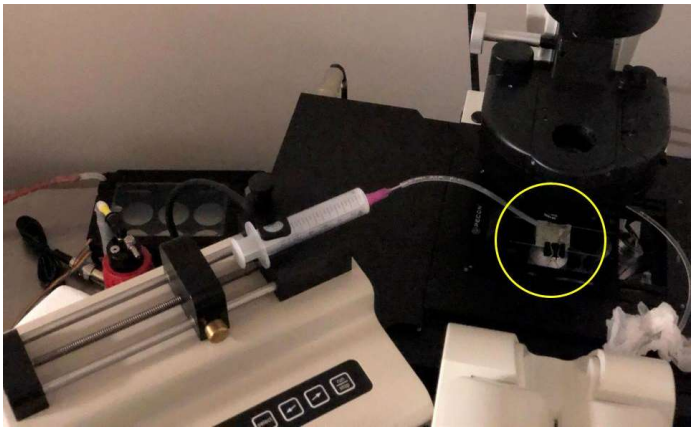

Fig. 2. Setup of 3D-printed prototype with syringe pump and microscope. The position of the 3D-printed device is indicated by the yellow circle.

End Matter

Author Contributions and Notes

T.B., M.C., and C.L. conceived the research and device design. C.L. ran CFD simulations and T.B. and M.C. ran device flow experiments. C.L. and T.B. created the CAD designs for soft-lithography and 3D-printing. T.B., M.C., and C.L. wrote the paper.

Acknowledgments

We'd like to thank Dr. Highley and Jack Whitewolf for their advice and mentorship throughout this project. We would also like to thank Dr. Allen and Dr. Barker for their efforts in teaching the Capstone class in the fall and spring semesters, as well as Kareem, Delaney, and Taylor for giving wonderful advice as Capstone TAs.

References

1. Benjamin Emelia J. et al. Heart Disease and Stroke Statistics—2019 Update: A Report From the American Heart Association. Circulation 139, e56–e528 (2019).
2. Hankey, G. J. Stroke. Lancet 389, 641–654 (2017).
3. Langhorne, P., Bernhardt, J. & Kwakkel, G. Stroke rehabilitation. The Lancet 377, 1693–1702 (2011).
4. Hashemi, M. & Kalalinia, F. Application of encapsulation technology in stem cell therapy. Life Sciences 143, 139–146 (2015).
5. Kim, S. U. & Vellis, J. de. Stem cell-based cell therapy in neurological diseases: A review. Journal of Neuroscience Research 87, 2183–2200 (2009).
6. Wei, L., Wei, Z. Z., Jiang, M. Q., Mohamad, O. & Yu, S. P. Stem cell transplantation therapy for multifaceted therapeutic benefits after stroke. Progress in Neurobiology 157, 49–78 (2017).
7. Savitz, S. I., Rosenbaum, D. M., Dinsmore, J. H., Wechsler, L. R. & Caplan, L. R. Cell transplantation for stroke. Ann Neurol 52, 266–275 (2002).
8. Bliss Tonya, Guzman Raphael, Daadi Marcel, & Steinberg Gary K. Cell Transplantation Therapy for Stroke. Stroke 38, 817–826 (2007).
9. Krishnan, R., Alexander, M., Robles, L., Foster 3rd, C. E. & Lakey, J. R. T. Islet and Stem Cell Encapsulation for Clinical Transplantation. Rev Diabet Stud 11, 84–101 (2014).
10. Vegas, A. J. et al. Long-term glycemic control using polymer-encapsulated human stem cell–derived beta cells in immune-competent mice. Nature Medicine 22, 306–311 (2016).
11. Zhao, S. et al. Bioengineering of injectable encapsulated aggregates of pluripotent stem cells for therapy of myocardial infarction. Nature Communications 7, 1–12 (2016).
12. Jiang, Z., Xia, B., McBride, R. & Oakey, J. A microfluidic-based cell encapsulation platform to achieve high long-term cell viability in photopolymerized PEGNB hydrogel microspheres. Journal of Materials Chemistry B 5, 173–180 (2017).
13. Liu, T. et al. Biomedical Applications of Layer-by-Layer Self-Assembly for Cell Encapsulation: Current Status and Future Perspectives. Advanced Healthcare Materials 8, 1800939 (2019).
14. Nasiri, R. et al. Microfluidic - Based Approaches in Targeted Cell/Particle Separation Based on Physical Properties: Fundamentals and Applications. Small 16, 2000171 (2020).

15. Zhang, J. et al. Fundamentals and applications of inertial microfluidics: a review. Lab Chip 16, 10–34 (2016).
16. Bhagat, A. A. S. et al. Microfluidics for cell separation. Med Biol Eng Comput 48, 999–1014 (2010).
17. Ying, Y. & Lin, Y. Inertial Focusing and Separation of Particles in Similar Curved Channels. Scientific Reports 9, 16575 (2019).
18. Xiang, N. et al. Precise Size-Based Cell Separation via the Coupling of Inertial Microfluidics and Deterministic Lateral Displacement. Anal Chem 91, 10328–10334 (2019).
19. Mach, A. J., Kim, J. H., Arshi, A., Hur, S. C. & Carlo, D. D. Automated cellular sample preparation using a Centrifuge-on-a-Chip. Lab Chip 11, 2827–2834 (2011).
20. Di Carlo, D., Irimia, D., Tompkins, R. G. & Toner, M. Continuous inertial focusing, ordering, and separation of particles in microchannels. Proc Natl Acad Sci U S A 104, 18892–18897 (2007).
21. Morales Navarrete, P. & Yuan, J. A Single-Layer PDMS Chamber for On-Chip Bacteria Culture. Micromachines 11, 395 (2020).

Supplemental Material

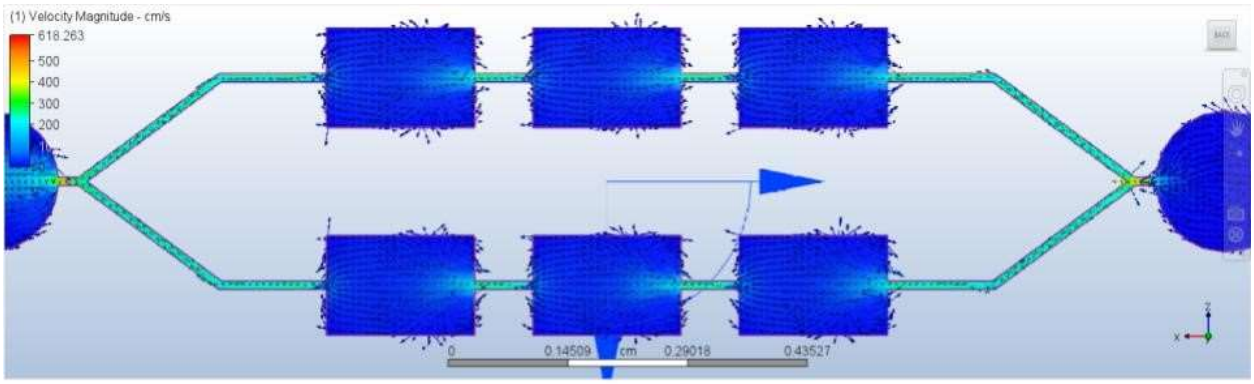

Supplemental Figure S1. Vector fields across inertial chambers in series and in parallel.

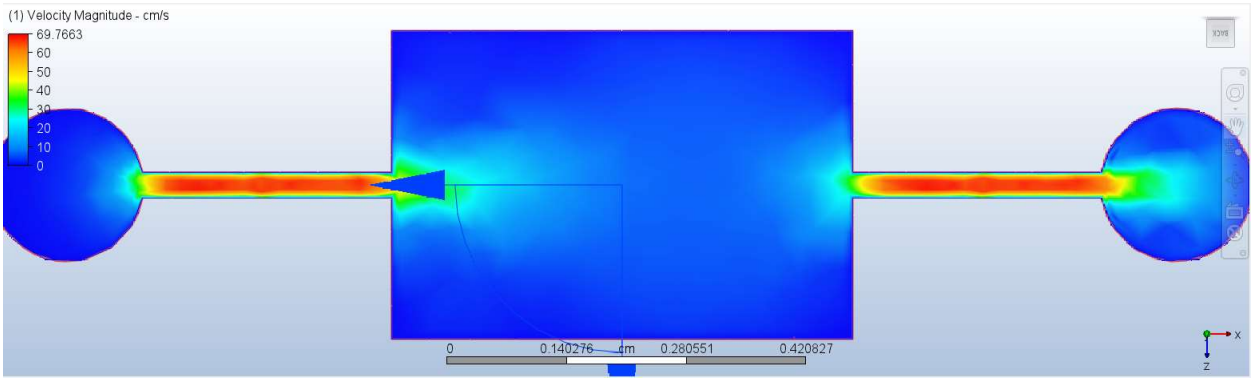

Supplemental Figure S2. Representative velocity heatmap used to calculate the velocity at specific points within the inertial chamber.

$$Re_c = \frac{\rho u L}{\mu} = \frac{\rho u^2}{\mu \frac{u}{L}} = \frac{uL}{v} \; ; \; L = d_h = \frac{2AB}{A+B} \; ; \; \rho = 1 \frac{g}{mL}$$

$$\Rightarrow \; Re_c = \frac{2uAB}{v(A+B)} \; ; \; v = \frac{\mu}{\rho} = \mu \; ; \; u = \bar{v} = \frac{Q}{AB}$$

$$\Rightarrow \; Re_c = \frac{2QAB}{\mu AB(A+B)} = \frac{2Q}{\mu(A+B)} \; ; \; \mu = 0.01 \frac{g}{cm*s}$$

$$\therefore \; Re_c = \frac{200Q}{A+B}$$

ρ : density (g/mL)
u : velocity based on cross-section (cm/s)
L : characteristic length (cm)
d_h : hydraulic diameter (cm)
μ : viscosity (g/cm/s)
v : kinematic viscosity (cm^2/s)
A & B : dimensions of channel (cm)
$\bar{v}$: average velocity (cm/s)
Q : volumetric flow (mL/s)

Supplemental Figure S3. Derivation of Reynolds number formula for rectangular inertial chamber.